Unconventional spin-orbit torque in transition metal dichalcogenide/ferromagnet bilayers from first-principles calculations

Fei Xue,[1,2] Christoph Rohmann,[1,2] Junwen Li,[3] Vivek Amin,[1,2] and Paul Haney[1]

[1] *Physical Measurement Laboratory, National Institute of Standards and Technology, Gaithersburg, MD 20899, USA*
[2] *Institute for Research in Electronics and Applied Physics & Maryland Nanocenter, University of Maryland, College Park, MD 20742*
[3] *DFTWorks LLC, Oakton, VA 22124*

(Dated: February 10, 2022)

Motivated by recent observations of unconventional out-of-plane dampinglike torque in WTe_2/Permalloy bilayer systems, we calculate the spin-orbit torque generated in two-dimensional transition metal dichalcogenide (TMD)-ferromagnet heterostructures using first-principles methods and linear response theory. Our numerical calculation of spin-orbit torques in WTe_2/Co and $MoTe_2$/Co heterostructures shows both conventional and novel dampinglike torkances (torque per electric field) with comparable magnitude, around $100\hbar/2e$ $(\Omega \cdot \mathrm{cm})^{-1}$, for an electric field applied perpendicular to the mirror plane of the TMD layer. To gain further insight into the source of dampinglike torque, we compute the spin current flux between the TMD and Co layers and find good agreement between the two quantities. This indicates that the conventional picture of dampinglike spin-orbit torque, whereby the torque results from the spin Hall effect plus spin transfer torque, largely applies to TMD/Co bilayer systems.

arXiv:2005.01109v2 [cond-mat.mes-hall] 6 Jul 2020

I. INTRODUCTION

Spin-orbit torque is an effect in which the application of an electric field induces the exchange of angular momentum between the crystal lattice and the magnetization of a magnetically ordered material[1–4]. This exchange is mediated by spin-orbit coupling, and the effect offers a promising mechanism for energy-efficient electrical switching of thin film ferromagnets. The prototypical geometry of a spin-orbit torque-based device is shown in Fig. 1: charge current is applied in the plane of a heavy metal-ferromagnet bilayer, leading to magnetic dynamics and potentially switching of the ferromagnetic orientation. This geometry is quite distinct from the conventional spin transfer torque-based magnetic tunnel junctions, which utilize spin-polarized current flowing perpendicular to the materials' interfaces[5]. The geometry of devices which utilize spin-orbit torque enables separate electrical paths for writing and reading the magnetic information, which may be advantageous for applications[6].

The dependence of the spin-orbit torque on the magnetization orientation is determined by the system symmetry. In many devices studied to date (*e.g.*, Co-Pt bilayers), the materials are deposited by sputtering and the film is effectively isotropic in the plane normal to the interface. This leaves the stacking direction ($\mathbf{z}$) as the only broken-symmetry direction. In the presence of an applied electric field $\mathbf{E}$, and for the magnetization aligned to the $\mathbf{E} \times \mathbf{z}$ direction, the system is invariant under reflections about the plane spanned by $\mathbf{E}$ and $\mathbf{z}$. This implies that the torque on the magnetization vanishes in this configuration, so that it is a fixed point for electric field-induced magnetic dynamics[7]. This in turn implies that the spin-orbit torque for such a system can deterministically switch the magnetization between in-plane configurations[6,8].

Breaking the in-plane symmetry of the system removes this constraint on the form of the torque. In this case, the electric field-induced torque generally drives the magnetization to a point above or below the plane of the film (depending on the current polarity). This enables deterministic switching of perpendicularly magnetized thin film ferromagnets. This is of particular interest due to technological advantages of perpendicularly magnetized layers, such as improved switching speed and efficiency[9,10]. The reduction of symmetry has been realized experimentally through a variety of means, such as the application of an in-plane magnetic field[3,11,12], the addition of in-plane magnetized layers (ferromagnetic[13,14] or antiferromagnetic[15,16]), or engineered structural asymmetry[17]. Of relevance to this work is a series of recent experiments in which substrates with reduced crystal symmetry (transition metal dichalcogenide) were utilized to realize spin-orbit torques with a form that enables switching of perpendicular ferromagnets[18–21].

While symmetry dictates the form of the spin-orbit torque, quantifying its magnitude and identifying its microscopic origin require explicit calculation. Knowledge of these properties can aid in developing materials and device selection rules in order to optimize relevant figures of merit, such as switching efficiency. With this motivation, we report on first-principles calculations of electric-field induced spin-orbit torque in transition metal dichalcogenide(TMD)-ferromagnet bilayers. Our numerical analysis demonstrates that a considerable out-of-plane dampinglike torque is generated in this low symmetry system. We also provide a general analysis of the symmetry-allowed torques for materials of this symmetry class. We compute the spin current flowing between layers in the heterostructure, and find that it provides the primary source of torque on the magnetic layer.

Our paper is organized as follows. In Sec. II we review

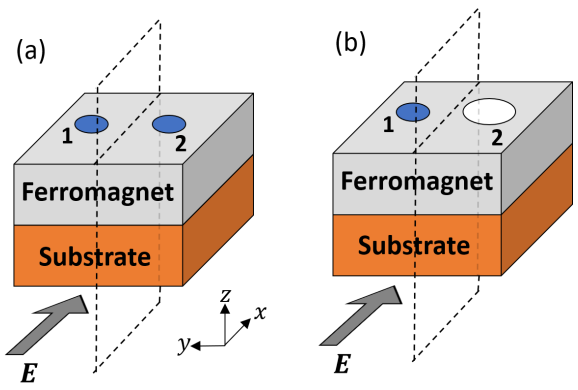


FIG. 1. (a) Schematic of heavy metal (substrate)-ferromagnet bilayer with in-plane 4-fold symmetry; atoms 1 and 2 are equivalent and the system retains $y \to -y$ symmetry when the magnetization is along the **y** direction. (b) Bilayer system with broken mirror symmetry; atoms 1 and 2 are inequivalent. For magnetization along the **y** direction, there are no system symmetries and all components of torque are allowed.

the procedure for computing spin-orbit torque using *ab initio* methods and linear response theory. In Sec. III we present and discuss results obtained from the first-principles calculation of dampinglike and fieldlike spin-orbit torque. In Sec. IV, we compare the torque to the spin current flux, and in Sec. V we present our conclusions.

II. COMPUTATIONAL METHODS

A. Formalism

The Hamiltonian of a magnetic system is generally given by the sum of a magnetization-dependent part and magnetization-independent part, which includes the kinetic energy T, potential energy V, and spin-orbit coupling. Within the local spin density approximation (LSDA), the magnetic order leads to a spin-dependent exchange-correlation potential $\mathbf{\Delta}$ which couples to electron spin $\mathbf{S}$ through an exchange interaction $\mathbf{\Delta} \cdot \hat{\mathbf{S}}$. We approximate the spin-orbit coupling with an on-site, atomic-like form $\hat{\mathbf{L}} \cdot \hat{\mathbf{S}}$[22]. The Hamiltonian is then given by:

$$H = T + V + \mathbf{\Delta} \cdot \hat{\mathbf{S}} + \alpha \hat{\mathbf{L}} \cdot \hat{\mathbf{S}}, \tag{1}$$

where $\hat{\mathbf{L}}$ and $\hat{\mathbf{S}}$ are (unitless) electron orbital angular momentum and spin Pauli matrices respectively, and α is a diagonal matrix parametrizing the spin-orbit coupling strength of different atoms. The torque operator $\boldsymbol{\mathcal{T}}$ is calculated from the change of magnetization with respect to time,

$$\boldsymbol{\mathcal{T}} = \frac{d\mathbf{\Delta}}{dt} = \frac{\mathrm{i}}{\hbar}[H, \mathbf{\Delta}] = -\frac{\mathrm{i}}{\hbar}[\mathbf{\Delta} \cdot \hat{\mathbf{S}}, \hat{\mathbf{S}}]. \tag{2}$$

When an external electric field is applied, the electron distribution function and wave function are both modified. The linear response from the change of the Fermi-Dirac distribution function is time-reversal odd within the relaxation time approximation[23], while the linear response from the change of electronic wave function is time-reversal even[24]. Using the Kubo formula[24–27], the even and odd torkances (the torque per electric field strength per area) under the external field in **x**-direction are expressed as

$$\boldsymbol{\tau}^{\mathrm{even}} = 2e \sum_{\substack{\mathbf{k},n \\ m \neq n}} f(E_{n\mathbf{k}}) \frac{\mathrm{Im}\, \langle \psi_{n\mathbf{k}} | \frac{dH}{dk_x} | \psi_{m\mathbf{k}} \rangle \langle \psi_{m\mathbf{k}} | \boldsymbol{\mathcal{T}} | \psi_{n\mathbf{k}} \rangle}{(E_{m\mathbf{k}} - E_{n\mathbf{k}})^2 + \eta^2}, \tag{3}$$

$$\boldsymbol{\tau}^{\mathrm{odd}} = \frac{e}{\pi} \sum_{\mathbf{k},n,m} \frac{\eta^2 \mathrm{Re}[\langle \psi_{m\mathbf{k}} | \frac{dH}{dk_x} | \psi_{n\mathbf{k}} \rangle \langle \psi_{n\mathbf{k}} | \boldsymbol{\mathcal{T}} | \psi_{m\mathbf{k}} \rangle]}{[(\mu - E_{n\mathbf{k}})^2 + \eta^2][(\mu - E_{m\mathbf{k}})^2 + \eta^2]}, \tag{4}$$

where $|\psi_{n\mathbf{k}}\rangle$ satisfy the steady-state Schrodinger equation, $H_{\mathbf{k}} |\psi_{n\mathbf{k}}\rangle = E_{n\mathbf{k}} |\psi_{n\mathbf{k}}\rangle$, and are labeled by Bloch wave vector $\mathbf{k}$ and band index n. In Eqs. 3-4, e is the electron charge, $f(E)$ is the equilibrium Fermi-Dirac distribution function, μ is the chemical potential, and η is the broadening parameter (note that f depends on μ). We use $k_B T = \eta = 25$ meV throughout the paper unless otherwise noted.

We assume H is expressed in a tight-binding representation. In evaluating Eqs. 3 and 4, the velocity matrix operator is given by $\frac{dH}{dk_{x,y}} = \sum_{\mathbf{R}} (\mathrm{i} R_{x,y}) e^{\mathrm{i}\mathbf{k}\cdot\mathbf{R}} H_{\mathbf{R}}$, where $H_{\mathbf{R}}$ is the Hamiltonian matrix coupling the orbitals centered in the primary unit cell with orbitals centered in the unit cell displaced by $\mathbf{R}$. We include the atomic coordinate positions (*i.e.*, the basis vectors of atoms within the unit cell) in the displacement vector $\mathbf{R}$[28]. Within the LSDA approximation, we can rotate the magnetization direction by rotating the time-reversal odd component of the real-space tight-binding Hamiltonian.

We also evaluate the spin current flowing between the two layers of the heterostructure, whose evaluation we describe next. We write the Hamiltonian for the bilayer system as:

$$H = \begin{pmatrix} H_{\mathrm{FM}} & t_{\mathrm{FM,TMD}} \\ t_{\mathrm{TMD,FM}} & H_{\mathrm{TMD}} \end{pmatrix} \tag{5}$$

The diagonal elements of Eq. 5 describe intralayer (or "on-site") contributions to the Hamiltonian. The off-diagonal elements describe the coupling (or "hopping") between layers. The interlayer electron current operator J is given by:

$$J = i \begin{pmatrix} 0 & t_{\mathrm{FM,TMD}} \\ -t_{\mathrm{TMD,FM}} & 0 \end{pmatrix}. \tag{6}$$

We denote the spin current flowing between layers as $\mathbf{Q}$, whose vector direction specifies the spin polarization of

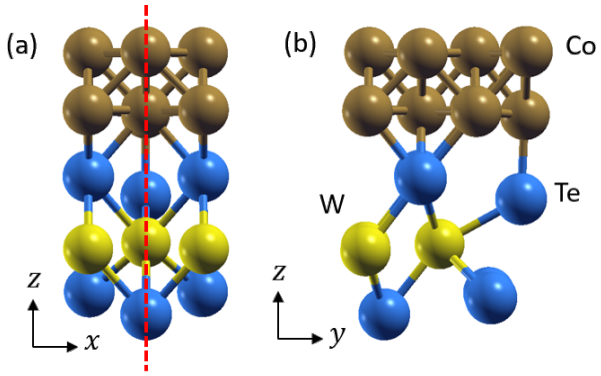


FIG. 2. Depiction of system geometry for $WTe_2(1)/Co(2)$. Note the system retains mirror symmetry about the yz plane ($x \to -x$), but breaks mirror symmetry about the xz plane.

the spin current. The spin current operator is the symmetrized product of the interlayer current and the spin operator:

$$Q_\alpha = \frac{1}{2}\left(\hat{S}_\alpha J + J\hat{S}_\alpha\right) \tag{7}$$

To evaluate the electric-field-induced spin current, we replace $\boldsymbol{\mathcal{T}}$ with $\mathbf{Q}$ in Eqs. 3 and 4[29].

B. First principles calculations

In this section we describe some details of the first principles calculations, which proceed in three steps: structural relaxation, Wannier projection, and evaluation of Eqs. 3 and 4 using the tight-binding Hamiltonian.

The structural relaxation itself is a two-step process, in which we first relax using the Vienna Ab initio Simulation Package (VASP)[3031], and use this relaxed structure as input to a second structural relaxation in Quantum ESPRESSO[32]. We find this is more efficient than exclusively using Quantum ESPRESSO for relaxation. In the VASP calculation, we use the PAW method[33] with the Perdew-Burke-Ernzerhof generalized-gradient approximation (PBE-GGA) functional[34]. All structures are relaxed until the total energy converges to within 10^{-4} eV during the self-consistent loop, with forces converged to 0.1 eV/nm, while employing the Methfessele-Paxton method with a smearing of 0.2 eV width. The Brillouin zone is sampled with a $7 \times 4 \times 1$ Monkhorst Pack mesh[35]. An energy cutoff of 450 eV is used for all calculations. Van der Waals interactions are accounted for by means of the Grimme (D2) scheme[36]. The valence electron configurations for each metal considered are W: $5d^5 6s^1$, Te: $5s^2 5p^4$, Co: $3d^8 4s^1$ and Mo: $4d^5 5s^1$.

Prior to creating the TMD/Co systems, the lattice constants of the isolated TMD layer are optimized, resulting in $a = 0.349$ nm, $b = 0.625$ nm for WTe_2 and $a = 0.348$ nm, $b = 0.636$ nm for $MoTe_2$. The Co-TMD heterostructure consists of 1-2 monolayers of TMD stacked on a Co slab 3 layers thick with 4 Co atoms per layer. There is a large mismatch between TMD and Co lattice constants. In this work, we apply most of the strain to the Co layer (see Fig. 2) since we focus on retaining the crystal symmetry of the TMD layer, and experimental samples exhibit a lack of crystallinity in the ferromagnetic layer[18,19,21] with amorphous Permalloy as the ferromagnet layer. More realistic treatments of the system would require a large TMD/Co unit cell to reduce the lattice mismatch. However such systems are not feasible due to the computational cost. To maintain the mirror symmetry ($x \to -x$) of the system a two-step optimization process is performed. In the first step all atomic positions are allowed to relax. In the following step the x positions of the Co atoms are aligned with those of W (Mo) and Te and restricted from movement (frozen), and the structure is relaxed again. The relaxed atomic positions are provided in Appendix B.

The relaxed structure provided by VASP serves as the initial configuration for the structural relaxation calculation in Quantum ESPRESSO. The optimized Co atoms form three flat layers consisting of 4 atoms per layer. To reduce the tight-binding system size and computational load, we remove the top Co layer prior to relaxation in Quantum ESPRESSO. The relaxation calculation is non-relativistic and spinpolarized, and utilizes a $12 \times 6 \times 1$ Monkhorst-Pack mesh[35], cutoff energy 1088 eV, total energy convergence threshold 1.36×10^{-3} eV, and force convergence threshold 2.57×10^{-2} eV/nm.

With the optimized geometry of the heterostructure and the corresponding self-consistent ground state computed with Quantum ESPRESSO, we use Wannier90[37] to obtain the real-space tight-binding model in the basis of atomic orbitals. We project onto d orbitals of transition metal atoms, s and p orbitals of chalcogen atoms, and s, p, d orbitals of Co atoms. After obtaining the collinear spin-polarized Hamiltonian in the Wannier basis, we add the onsite spin-orbit coupling terms $\alpha\hat{\mathbf{L}} \cdot \hat{\mathbf{S}}$. Note that adding spin-orbit coupling "by hand" in this manner requires that Wannier orbitals are not localized, in order to ensure that they are spherical harmonics consistent with the standard representation of $\mathbf{L}$. The strength of the spin-orbit coupling parameter α is obtained by fitting the pristine spin-orbit coupled bands from Quantum ESPRESSO. We obtain $\alpha = [350, 100, 500, 70]$ meV for W, Mo, Te, and Co, respectively. We adopt this approach because it is technically easier to achieve a good Wannier projection of a collinear magnetized Hamiltonian, and the on-site spin-orbit coupling approximation yields accurate results. Note that the Wannier projection procedure breaks the mirror symmetry slightly, so we manually restore the mirror symmetry using procedures as described in Ref.[38]. We use a k mesh of approximately 540×300 (similar integration steps in the $k_x(k_y)$ direction) to evaluate Eqs. 3 and 4.

III. RESULTS

A. Symmetry considerations

We preface the presentation of numerical results with a review of the symmetry properties of the system, which have been discussed in previous works[18,19,21]. In Appendix A, we present the fully general form of the current-induced torques for this system. In what follows we focus on the azimuthal angle dependence for in-plane magnetization orientations (along the equator of Fig. 3). We denote the out-of-plane and in-plane torques as follows:

$$\mathcal{T}_\perp = \mathcal{T}_z \tag{8}$$
$$\mathcal{T}_\parallel = \mathcal{T}_x \sin(\phi) - \mathcal{T}_y \cos(\phi), \tag{9}$$

where the azimuthal angle ϕ defines the in-plane magnetization direction: $M_x = M\cos\phi, M_y = M\sin\phi$. By examining the symmetry transformation of $\mathcal{T}_\perp$ and $\mathcal{T}_\parallel$ under an external field in the $\mathbf{x}$ direction, we find that both in-plane and out-of-plane torkances are cosine functions. We group them into time-reversal even and odd parts:

$$\begin{aligned}\tau_\perp &= \sum_{n=0}^{\infty} B_{2n}^{\perp,\text{even}} \cos(2n\phi) + B_{2n+1}^{\perp,\text{odd}} \cos\big((2n+1)\phi\big) \\ \tau_\parallel &= \sum_{n=0}^{\infty} B_{2n}^{\parallel,\text{odd}} \cos(2n\phi) + B_{2n+1}^{\parallel,\text{even}} \cos\big((2n+1)\phi\big)\end{aligned} \tag{10}$$

In this work we use the terms "time-reversal even torque" and "dampinglike torque" interchangeably, and also use the terms "time-reversal odd torque" and "fieldlike torque" interchangeably. The 1st order contribution to the in-plane time-reversal even torque ($B_1^{\parallel,\text{even}}$) is equivalent to the conventional dampinglike torque form, i.e., $\mathbf{M}\times\mathbf{M}\times(\mathbf{E}\times\mathbf{z})$, and the 0th order contribution to the out-of-plane time-reversal even torque ($B_0^{\perp,\text{even}}$) is the unconventional torque allowed only in the absence of mirror symmetry about the xz plane.

For an applied electric field in the $\mathbf{y}$-direction, the torques take the form

$$\begin{aligned}\tau_\perp &= \sum_{n} A_{2n}^{\perp,\text{even}} \sin(2n\phi) + A_{2n+1}^{\perp,\text{odd}} \sin\big((2n+1)\phi\big) \\ \tau_\parallel &= \sum_{n} A_{2n}^{\parallel,\text{odd}} \sin(2n\phi) + A_{2n+1}^{\parallel,\text{even}} \sin\big((2n+1)\phi\big)\end{aligned} \tag{11}$$

For this direction of $\mathbf{E}$ field, mirror symmetry about the yz plane is retained, and the torques assume a more conventional form. In particular there is no magnetization-independent out-of-plane dampinglike torque.

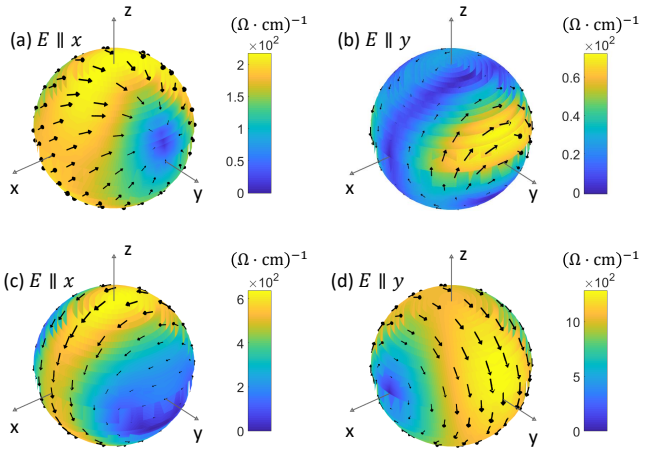


FIG. 3. (Color online) Angular dependence of the dampinglike (a and b) and fieldlike (c and d) torkance on the magnetization direction (θ,ϕ) for $WTe_2(1)/Co(2)$ under an external electric field along the $\hat{x}$ (a and c) and $\hat{y}$ (b and d) direction at Fermi level. The heterostructure system keeps the mirror symmetry $x\to -x$ only. The arrow(color) on the sphere indicates the direction(magnitude) of the torkance under the given magnetization direction.

B. Numerical Results

We next turn to the calculation results. Fig. 3 shows the torque as a function of magnetization orientation for a heterostructure composed of one WTe_2 layer and two layers of Co (as shown in Fig. 2). Figs. 3(a) and (c) show the dampinglike and fieldlike components of torque, respectively, for $\mathbf{E}$ along $\mathbf{x}$. Recall that for this direction of $\mathbf{E}$, all symmetries are broken and the form of the torque is unconstrained. The dampinglike torque drives the magnetization into a point in the yz plane. As discussed in the introduction, for this case an applied electric field can deterministically switch a perpendicularly magnetized layer due to the dampinglike torque driving the magnetization to a point in the northern or southern hemisphere. The fieldlike torque also vanishes at a point in the yz plane, although at a point different than for which the dampinglike torque vanishes. There is therefore no point at which the total electric-field-induced torque vanishes.

Figs. 3(b) and (d) show the same data for $\mathbf{E}$ along $\mathbf{y}$. This is a more conventional configuration in which there is a mirror plane symmetry with respect to the plane formed by $\mathbf{z}$ and $\mathbf{E}$. The dampinglike torque drives the magnetization into the $\mathbf{x}$ direction and vanishes there due to the mirror symmetry $x\to -x$. However we note that the dampinglike torque has substantial contributions from higher-order terms, and is not well described by the lowest-order form $(\mathbf{M}\times\mathbf{M}\times\mathbf{x})$[39,40]. The fieldlike torque is well described by the simple form $\mathbf{M}\times\mathbf{x}$.

We next consider a series of systems in which we vary

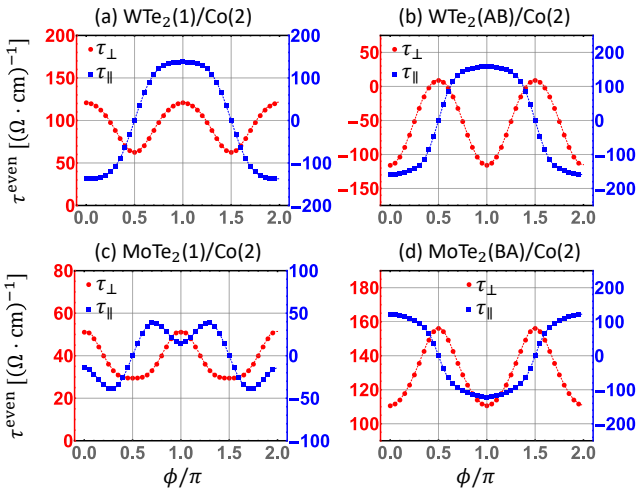


FIG. 4. (Color online) Azimuthal angle(ϕ) dependence of torkances for (a)WTe_2(1)/Co(2), (b)WTe_2(AB)/Co(2), (c)$MoTe_2$(1)/Co(2), (d)$MoTe_2$(2)/Co(2) at Fermi level. Red circles and blue squares denote out-of-plane torkance $\tau_\perp \equiv \tau_z$ and in-plane torkance $\tau_\parallel \equiv \tau_x \sin(\phi) - \tau_y \cos(\phi)$, respectively. Dashed lines show the fitted results based on the symmetry-constrained form Eq. 10 up to $n = 9$.

the TMD material type and thickness. We restrict our attention to the torque as a function of azimuthal angle ϕ for in-plane magnetization directions, and only consider $\mathbf{E}$ along $\mathbf{x}$. Fig. 4 shows $\tau_\parallel$, $\tau_\perp$ versus ϕ for 1 and 2 layers of WTe_2, and 1 and 2 layers of $MoTe_2$, all with 2 layers of Co. For the WTe_2 structures, going from 1 to 2 layers changes the sign of the out-of-plane torque $\tau_\perp$ and decreases its magnitude. This is consistent with experimental observations[19], and indicates that, not surprisingly, the sign of $\tau_\perp$ is determined by the direction of in-plane symmetry breaking of the interfacial layer. Consistent with this, we find that changing the order of stacking of WTe_2 from AB to BA changes the sign of the out-of-plane torque (see Fig. 5 for our definition of AB and BA stacking). AB and BA stacking cases are *approximately* equivalent up to a mirror symmetry which flips the polarity of in-plane-symmetry-breaking order; however there are small differences resulting from the structural relaxation (the detailed atom locations of are provided in App. B). The reduction in magnitude for $\tau_\perp$ with additional layers of WTe_2 can be expected because the two layers have opposite orientations of in-plane symmetry breaking. The out-of-plane torque due to the two layers should therefore exhibit partial cancellation, leading to a reduction in the overall magnitude. We find that $\tau_\parallel$ is relatively insensitive to the WTe_2 thickness.

For the $MoTe_2$ structures, we find somewhat different behavior: $\tau_\perp$ and $\tau_\parallel$ both increase in magnitude going from 1 to 2 layers of $MoTe_2$. It is surprising that $\tau_\perp$ increases with 2 layers, in light of the expected partial cancellation due to layers with opposite in-plane symmetry breaking, as described in the previous paragraph. However, the torque is quite sensitive to other features of the structure, which we discuss later. Note that we do not calculate another AB stacking case of $MoTe_2$ for simplicity since this will be similar to what we find in WTe_2.

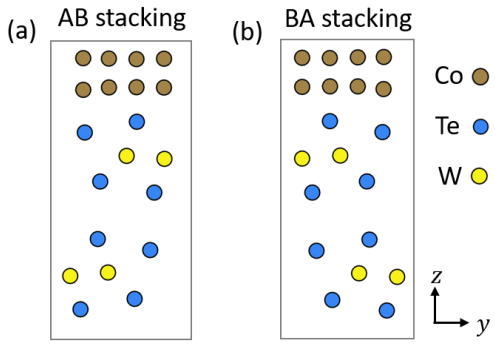


FIG. 5. Panels (a) and(b) depict the atomic configurations for AB and BA stacking, respectively.

We fit our first-principles numerical results with the symmetry-constrained forms (Eq. 10) to extract the values of out-of-plane and in-plane torkances for five structures. The two lowest-order torkance conductivities are summarized in Table. I. Our numerical data conform to the symmetry-constrained forms with a sizable magnitude of constant out-of-plane torkance. Note that the numerical data contain small but finite symmetry-allowed higher-order terms such as $\cos(2\phi)$ in the out-of-plane torkance.

To test the robustness of the computed torkance values with respect to disorder, we utilize an Anderson disorder treatment[39] by adding a uniformly distributed random onsite potential $-V_m < V_i < V_m$ on all Co atoms. Fig. 6 shows the torkance coefficients versus Fermi energy for 40 realizations of random on-site potentials for the WTe_2(1)/Co(2) system. We find that adding a uniformly distributed random onsite potential with relatively small magnitude (100 meV) has a notable impact on the computed value. The mean and standard deviation of the computed values are shown for WTe2(1)/Co(2) in Table I. The standard deviation is substantial compared to the mean, underscoring the sensitivity of the computed values to details of the system. Note that we keep the

	$WTe_2(1)/Co(2)$	$WTe_2(AB)/Co(2)$	$WTe_2(BA)/Co(2)$	$MoTe_2(1)/Co(2)$	$MoTe_2(BA)/Co(2)$
$B_0^{\perp,\text{even}}$	84± 50	-52	40	39	131
$B_2^{\perp,\text{even}}$	30± 28	-63	65	11	-22
$B_1^{\parallel,\text{even}}$	-146±68	-181	-180	-35	135
$B_3^{\parallel,\text{even}}$	15± 14	28	23	19	-18
$B_1^{\perp,\text{odd}}$	-301±410	922	1165	-1973	-199
$B_3^{\perp,\text{odd}}$	-115±77	86	-83	-30	-88
$B_0^{\parallel,\text{odd}}$	57±380	-329	238	370	624
$B_2^{\parallel,\text{odd}}$	-107±81	74	-79	-56	-29

TABLE I. Table of fitting parameters based on Eq. 10 in five different heterostructures, given in units of $\hbar/2e\ (\Omega\cdot\text{cm})^{-1}$. For the $WTe_2(1)$ /Co(2), we add an error bar from the Anderson disorder treatment described in the text. $WTe_2(BA)/Co(2)$ and $WTe_2(1)/Co(2)$ share a similar interfacial geometry (*i.e.*, the same direction of in-plane symmetry breaking).

chemical potential constant in different disorder realizations. Increasing V_m to 200 meV results in similar values of torkance ($B_0^{\perp,\text{even}} = 94\pm64\ \hbar/2e\ (\Omega\cdot\text{cm})^{-1}$, $B_2^{\perp,\text{even}} = 32\pm56\ \hbar/2e\ (\Omega\cdot\text{cm})^{-1}$). Clearly, disorder plays an important role; however, a systematic study of the dependence of torkance on disorder is beyond the scope of the current paper.

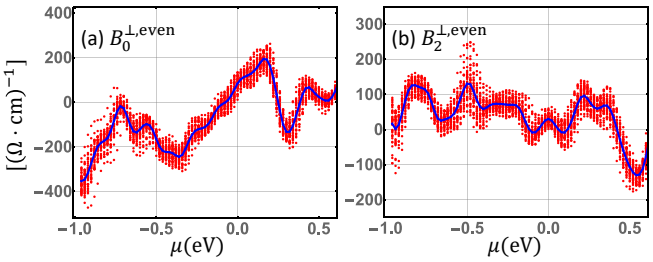


FIG. 6. (Color online) Fitted parameters in $WTe_2(1)/Co(2)$ as a function of chemical potential for 40 random onsite potentials $-0.1\text{ eV} < V_i < 0.1\text{ eV}$ on all Co atoms. Panels (a) and (b) show lowest ($B_0^{\perp,\text{even}}$) and second-lowest ($B_2^{\perp,\text{even}}$) order terms for out-of-plane torque. Red dots denote all 40 possible outcomes at each chemical potential (relative to the Fermi energy) and blue lines show the average of all variations.

IV. TORQUE AND SPIN CURRENT

In heavy metal-ferromagnet bilayers, the dampinglike spin-orbit torque is conventionally viewed as a consequence of the spin current generated in the heavy metal through the spin Hall effect, which flows into the ferromagnet thereby exerting a torque on the magnetization. First-principles calculations have shown that for Co-Pt bilayer systems, the dampinglike torque is indeed nearly equal to the spin current flux flowing between Pt and Co layers[24,39,41]. Recent work has shown that there are other sources for spin-orbit torque[42], such as the orbital Hall effect in the nonmagnet[43,44], anomalous torque in the ferromagnet[45], and interfacial torque[1,46]. We next perform calculations to determine which mechanism applies for this set of systems.

Fig. 7 shows that the torque on orbitals centered in the Co layer is approximately equal to the total torque, and, for most Fermi energies, also approximately equal to the spin current flux. There are regions of discrepancy between torque and spin current flux, particularly for the in-plane dampinglike torque $\tau_\parallel$ at higher Fermi energy. We find that for this case, the difference between spin current and torque is due to spin-orbit coupling on the Co atoms, which acts as a drain on spin angular momentum and diverts incoming spin current into torque on the lattice[42,47]. However generally there is good agreement between the spin current flux and the torque. This indicates that the conventional picture of dampinglike torque arising from spin current flux generated in the substrate is generally applicable for this system.

We note that the values obtained for the conventional dampinglike torque $B_1^{\parallel,\text{even}}$ are similar in magnitude to the bulk spin Hall conductivity computed for WTe_2 and $MoTe_2$[48]. In the spin current + spin transfer torque picture, the unconventional out-of-plane dampinglike torque would arise from spin current flowing along the **z**-direction (or *c*-axis of the TMD), with spin polarization along the **z**-axis. As shown in Ref[18], this component of the bulk spin Hall conductivity is symmetry-forbidden in crystals with the symmetry of WTe_2. However, the non-symmorphic screw symmetry allows for a bulk spin current whose spin polarization along **z** alternates in sign between subsequent TMD layers (*i.e.*, a staggered spin current). This staggered response has been discussed in general terms in Ref.[49], and realized in various contexts, such as in the staggered Rashba-Edelstein effect present in CuMnAs[50]. We have performed preliminary calculations of this staggered out-of-plane spin Hall conductivity for bulk WTe_2 and $MoTe_2$ and compute conductivities which, although smaller than spin-orbit torque $B_0^{\perp,\text{even}}$, are within the same order of a few tens of $(\hbar/2e)\ (\Omega\cdot\text{cm})^{-1}$. We leave this detailed analysis for future work. The correspondence between torque and spin current indicates that maximizing the substrate material's bulk spin Hall conductivity is a viable strategy for maximizing the spin-orbit torque in the

corresponding heterostructure.

The overall magnitude of the unconventional dampinglike torque we compute (see Table I) is quite similar to the experimentally observed value of (36 ± 8) $(\hbar/2e)$ $(\Omega \cdot \mathrm{cm})^{-1}$[18]. This is substantially less than the value of dampinglike torque commonly observed and computed for the more conventional Co-Pt system, which is in the range 10^3 $(\hbar/2e)$ $(\Omega \cdot \mathrm{cm})^{-1}$[7,11,24,51,52]. In light of the correspondence between spin current and spin-orbit torque described above, this difference can be understood as a consequence of the relatively moderate magnitude of bulk spin Hall conductivity in WTe_2[48]. We hypothesize that this is traced back to the large distance between successive TMD layers along the c axis, but again leave a systematic analysis for future work. We also note recent work which demonstrated magnetic switching using WTe_2 substrates[53], indicating that the conventional dampinglike torque in these materials may be sufficiently strong for applications. The magnitude of fieldlike torque we compute is also similar to that seen experimentally[54,55].

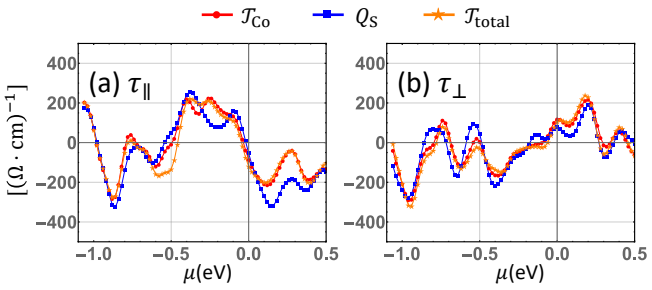


FIG. 7. (a) In-plane torque $\tau_\parallel$ on Co-centered orbitals, total torque, and spin current with y polarization flowing between TMD and Co layers as a function of chemical potential. (b) Same data for out-of-plane component of torque $\tau_\perp$ and spin current with z polarization. The electric field and magnetization are in the **x** direction.

V. CONCLUSION

In this work we presented first-principles calculations of the spin-orbit torque in a variety of TMD-Co bilayer systems. As expected, the reduced symmetry of the TMD substrate enables novel forms of the spin-orbit torque, which can enable the deterministic switching of perpendicularly magnetized thin-film ferromagnets. We find a magnitude of the dampinglike spin-orbit torque which is consistent with experiment, and substantially less than that found in more commonly studied systems such as Co-Pt bilayers. We also find that the spin-orbit torque is approximately equal to the spin current flux flowing from TMD layer to ferromagnetic layer, whose value is also commensurate with calculations of bulk spin Hall conductivity in TMD such as WTe_2 and $MoTe_2$. This suggests that maximizing the out-of-plane dampinglike torque may be accomplished by choosing substrate materials with large values of bulk out-of-plane spin-polarized spin Hall conductivity.

VI. ACKNOWLEDGMENT

F.X. acknowledges support under the Cooperative Research Agreement between the University of Maryland and the National Institute of Standards and Technology Physical Measurement Laboratory, Award 70NANB14H209, through the University of Maryland.

Appendix A: General symmetry analysis

In this appendix we present the general form for the current-induced torque for a bilayer system whose only symmetry operation is mirror symmetry about the yz plane.

1. Symmetry-constrained effective magnetic field

Assume that an applied electric field ($\mathbf{E}$) gives rise to an effective magnetic field ($\mathbf{B}$) in a ferromagnetic system. To linear order in electric field, the response is given by

$$\mathbf{B} = \chi(\hat{\mathbf{m}})\mathbf{E} \tag{A1}$$

where χ is a 3×3 tensor that depends on the magnetization direction $\hat{\mathbf{m}} = \left(\sqrt{1-z^2}\cos(\phi), \sqrt{1-z^2}\sin(\phi), z\right)$. The torque on the magnetization is given by

$$\tau = \hat{\mathbf{m}} \times \mathbf{B} \tag{A2}$$

Since the unit vector $\hat{\mathbf{m}}$ is parameterized by z and ϕ, the general response tensor can be written as

$$\chi(z,\phi) = \begin{pmatrix} \chi_{11}(z,\phi) & \chi_{12}(z,\phi) & \chi_{13}(z,\phi) \\ \chi_{21}(z,\phi) & \chi_{22}(z,\phi) & \chi_{23}(z,\phi) \\ \chi_{31}(z,\phi) & \chi_{32}(z,\phi) & \chi_{33}(z,\phi) \end{pmatrix} \tag{A3}$$

Each component can be expanded in terms of real spherical harmonics,

$$\chi_{ij}(z,\phi) = \sum_{l=0}^{\infty}\sum_{m=0}^{l} P_l^m[z]\left(\alpha_{l,ij}^m \cos(m\phi) + \beta_{l,ij}^m \sin(m\phi)\right) \tag{A4}$$

where $\alpha_{l,ij}^m$ and $\beta_{l,ij}^m$ are constant coefficients and P_l^m are the associated Legendre polynomials. We rewrite this expression for convenience as

$$\chi(z,\phi) = \sum_{l=0}^{\infty}\sum_{m=0}^{l} c_l^m(z,\phi)A_l^m + s_l^m(z,\phi)B_l^m \tag{A5}$$

where

$$c_l^m(z,\phi) = P_l^m[z]\cos(m\phi) \tag{A6}$$
$$s_l^m(z,\phi) = P_l^m[z]\sin(m\phi) \tag{A7}$$

and

$$A_l^m = \begin{pmatrix} \alpha_{l,11}^m & \alpha_{l,12}^m & \alpha_{l,13}^m \\ \alpha_{l,21}^m & \alpha_{l,22}^m & \alpha_{l,23}^m \\ \alpha_{l,31}^m & \alpha_{l,32}^m & \alpha_{l,33}^m \end{pmatrix}, \quad B_l^m = \begin{pmatrix} \beta_{l,11}^m & \beta_{l,12}^m & \beta_{l,13}^m \\ \beta_{l,21}^m & \beta_{l,22}^m & \beta_{l,23}^m \\ \beta_{l,31}^m & \beta_{l,32}^m & \beta_{l,33}^m \end{pmatrix}. \tag{A8}$$

The purpose of rewriting the response tensor was to separate the functional dependence on magnetization direction (z,ϕ) with the matrix structure (A_l^m,B_l^m).

2. Transforming the response tensor

In general, the response tensor transforms under some orthogonal transformation matrix R as follows:

$$\chi' = \det[R] R\chi R^{\mathrm{T}}. \tag{A9}$$

The yz mirror plane transformation (i.e. $x \to -x$ for polar vectors) is given by

$$R = \begin{pmatrix} -1 & 0 & 0 \\ 0 & 1 & 0 \\ 0 & 0 & 1 \end{pmatrix} \tag{A10}$$

Under this transformation, χ becomes

$$\chi' = -R\chi R^T = \begin{pmatrix} -\chi_{11} & \chi_{12} & \chi_{13} \\ \chi_{21} & -\chi_{22} & -\chi_{23} \\ \chi_{31} & -\chi_{32} & -\chi_{33} \end{pmatrix} \tag{A11}$$

To transform functions of magnetization, we note that the magnetization transforms like a pseudovector, which means that for a yz mirror plane transformation, $z' = -z$ and $\phi' = -\phi$. Thus,

$$c_l^m(z',\phi') = P_l^m[-z]\cos(-m\phi) = (-1)^{l+m} c_l^m(z,\phi) \tag{A12}$$
$$s_l^m(z',\phi') = P_l^m[-z]\sin(-m\phi) = -(-1)^{l+m} s_l^m(z,\phi) \tag{A13}$$

where we have used the identity $P_l^m[-z] = (-1)^{l+m} P_l^m[z]$. To obtain the symmetrized response tensor, we simply add the transformed tensor to the original tensor, since R and $I_{3\times3}$ are the only members of the symmetry group:

$$\begin{aligned} \chi_S(z,\phi) &= \chi(z,\phi) + \chi'(z',\phi') \\ &= \sum_{l=0}^{\infty}\sum_{m=0}^{l} c_l^m(z,\phi)\Big(A_l^m + (-1)^{l+m+1} R A_l^m R^T\Big) + \\ &\qquad s_l^m(z,\phi)\Big(B_l^m + (-1)^{l+m} R B_l^m R^T\Big) \end{aligned} \tag{A14}$$

3. Condensed form of response tensor

The response tensor derived in the last section contains matrices given by $A_l^m + (-1)^{l+m+1} R A_l^m R^T$ and $B_l^m + (-1)^{l+m} R B_l^m R^T$. Depending on the value of l and m, these matrices take either of the following forms:

$$S_l^m = \begin{pmatrix} a_l^m & 0 & 0 \\ 0 & e_l^m & f_l^m \\ 0 & h_l^m & i_l^m \end{pmatrix} \quad T_l^m = \begin{pmatrix} 0 & b_l^m & c_l^m \\ d_l^m & 0 & 0 \\ g_l^m & 0 & 0 \end{pmatrix} \tag{A15}$$

Using this observation, we can rewrite the response tensor one last time in matrix form as

$$\chi_S(z,\phi) = \sum_{l=0}^{\infty}\sum_{m=0}^{l} P_l^m[z]\big(s_l^m(\phi) S_l^m + t_l^m(\phi) T_l^m\big) \tag{A16}$$

where

$$s_l^m(\phi) = \begin{cases} \cos(m\phi) & \text{for } l,m = \text{even/odd or odd/even} \\ \sin(m\phi) & \text{for } l,m = \text{even/even or odd/odd} \end{cases} \tag{A17}$$

$$t_l^m(\phi) = \begin{cases} \sin(m\phi) & \text{for } l,m = \text{even/odd or odd/even} \\ \cos(m\phi) & \text{for } l,m = \text{even/even or odd/odd} \end{cases}. \tag{A18}$$

We have arrived at the final form of the general response tensor. For a given l and m, the contribution to each element of χ contains either $\sin(m\phi)$ or $\cos(m\phi)$ but not both. This is the main consequence of the symmetry $x \to -x$. Note that the matrix T_0^0 gives the magnetization-independent contribution ($l = 0, m = 0$) to χ. In general, the matrices S_l^m and T_l^m are odd and even with respect to the mirror plane transformation $x \to -x$ respectively.

4. Symmetry-constrained torque

The torque can be written in terms of its own response tensor χ^T defined as follows

$$\tau = \hat{\mathbf{m}} \times \mathbf{B} \tag{A19}$$
$$= \hat{\mathbf{m}} \times \chi\mathbf{E} \tag{A20}$$
$$= \chi^T\mathbf{E} \tag{A21}$$

where $\chi_{il}^T = \epsilon_{ijk}\hat{m}_j\chi_{kl}$. Replacing the coordinate z with θ, where $z = \cos(\theta)$, one can then show that

$$\chi^T(\theta,\phi)=\sum_{l=0}^{\infty}\sum_{m=0}^{l}P_l^m[\cos(\theta)]\Big(a_l^m A_l^m(\theta,\phi)+e_l^m E_l^m(\theta,\phi)+h_l^m H_l^m(\theta,\phi)+b_l^m B_l^m(\theta,\phi)+d_l^m D_l^m(\theta,\phi)+g_l^m G_l^m(\theta,\phi)\Big) \tag{A22}$$

where (assuming an in-plane electric field, i.e., $E_z=0$)

$$A_l^m=s_l^m(\phi)\begin{pmatrix}0 & 0 & 0\\ \cos(\theta) & 0 & 0\\ -\sin(\theta)\sin(\phi) & 0 & 0\end{pmatrix}\quad E_l^m=s_l^m(\phi)\begin{pmatrix}0 & -\cos(\theta) & 0\\ 0 & 0 & 0\\ 0 & \sin(\theta)\cos(\phi) & 0\end{pmatrix}\quad H_l^m=s_l^m(\phi)\begin{pmatrix}0 & \sin(\theta)\sin(\phi) & 0\\ 0 & -\sin(\theta)\cos(\phi) & 0\\ 0 & 0 & 0\end{pmatrix} \tag{A23}$$

$$B_l^m=t_l^m(\phi)\begin{pmatrix}0 & 0 & 0\\ 0 & \cos(\theta) & 0\\ 0 & -\sin(\theta)\sin(\phi) & 0\end{pmatrix}\quad D_l^m=t_l^m(\phi)\begin{pmatrix}-\cos(\theta) & 0 & 0\\ 0 & 0 & 0\\ \sin(\theta)\cos(\phi) & 0 & 0\end{pmatrix}\quad G_l^m=t_l^m(\phi)\begin{pmatrix}\sin(\theta)\sin(\phi) & 0 & 0\\ -\sin(\theta)\cos(\phi) & 0 & 0\\ 0 & 0 & 0\end{pmatrix} \tag{A24}$$

Note that the assumption of an in-plane electric field means that the coefficients c_l^m, f_l^m, and i_l^m are no longer relevant to the torque. The expansion provided here captures all the consequences of symmetry, but is obviously quite complicated because there are only two symmetry operations in the symmetry group. For each l and m, there are six independent parameters given by a_l^m, e_l^m, h_l^m, b_l^m, d_l^m, and g_l^m. The functions that contain the magnetization dependence are labeled accordingly.

5. Simpler expression for the out-of-plane torque

An out-of-plane (z) torque of some kind is required to switch ferromagnetic layers with perpendicular magnetic anisotropy. In the low-symmetry system we have studied here, such out-of-plane torques are nonvanishing. For an in-plane magnetization (i.e., $\theta=\pi/2$), the response tensor element relating an electric field along $\hat{\mathbf{x}}$ with the out-of-plane torque τ_z is

$$\chi_{zx}^T(\pi/2,\phi)=\sum_{l=0}^{\infty}\sum_{m=0}^{l}P_l^m[0]\big(a_l^m A_{l,zx}^m(\pi/2,\phi)+d_l^m D_{l,zx}^m(\pi/2,\phi)\big) \tag{A25}$$

$$=\sum_{l=0}^{\infty}\sum_{m=0}^{l}P_l^m[0]\big(-a_l^m s_l^m(\phi)\sin(\phi)+d_l^m t_l^m(\phi)\cos(\phi)\big), \tag{A26}$$

where we have used Eqs. A22, A23, and A24. We note that $P_l^m[0]$ is nonzero only when l and m are both even or both odd, which gives

$$\chi_{zx}^T(\pi/2,\phi)=\sum_{l=0}^{\infty}\sum_{m}^{l}\big(-a_l^m\sin(m\phi)\sin(\phi)+d_l^m\cos(m\phi)\cos(\phi)\big) \tag{A27}$$

$$=\sum_{l=0}^{\infty}\sum_{m}^{l}\frac{1}{2}\big((d_l^m+a_l^m)\cos((m+1)\phi)+(d_l^m-a_l^m)\cos((m-1)\phi)\big) \tag{A28}$$

where $s_l^m(\phi)$ and $t_l^m(\phi)$ are replaced with $\sin(m\phi)$ and $\cos(m\phi)$ in the first line using Eqs. A17 and A18. The last line is obtained using trigonometric summation identities. Note the second summation operator runs only over even (odd) values of m for even (odd) values of l.

Finally, we note that the above expression contains several redundancies, because the l dependence has dropped out and all integer multiples of ϕ are present somewhere in the sum. This yields

$$\chi_{zx}^T(\pi/2,\phi)=\sum_{m=0}^{\infty}n_m\cos(m\phi) \tag{A29}$$

where we have absorbed the redundant sums over coefficients a_l^m and d_l^m into n_m.

Appendix B: Notes on First principles calculations details

The atomic configurations of the relaxed structures are shown in the following tables. The unit of length for lattices vectors a_i is the angstrom, and fractional coordinates are shown.

TABLE II. Atomic Positions of WTe_2(1)/Co(2) and $MoTe_2$(1)/Co(2)

a_1	3.4895	0	0	a_1	3.4814	0	0
a_2	0	6.254	0	a_2	0	6.3562	0
a_3	0	0	45	a_3	0	0	39.9653
W	0.0	0.0608	0.2651	Mo	0.0	0.3244	0.3805
W	0.5	0.4169	0.2615	Mo	0.5	0.6915	0.3771
Te	0.0	0.6639	0.2954	Te	0.5	0.4256	0.4289
Te	0.5	0.1541	0.3088	Te	0.0	0.9346	0.4148
Te	0.0	0.3212	0.2170	Te	0.5	0.0750	0.3428
Te	0.5	0.8085	0.2311	Te	0.0	0.5872	0.3278
Co	0.5	0.3240	0.1720	Co	0.5	1.0842	0.2804
Co	0.0	0.5821	0.1720	Co	0.5	0.5885	0.2784
Co	0.5	0.8215	0.1755	Co	0.0	0.3277	0.2791
Co	0.0	0.0642	0.1727	Co	0.0	0.8452	0.2775
Co	0.0	0.3218	0.1354	Co	0.5	0.3318	0.2370
Co	0.0	0.8239	0.1340	Co	0.0	0.5837	0.2374
Co	0.5	0.5827	0.1344	Co	0.5	0.8424	0.2359
Co	0.5	0.0643	0.1351	Co	0.0	1.0892	0.2356

TABLE III. Atomic Positions of WTe_2(AB)/Co(2),WTe_2(BA)/Co(2), and $MoTe_2$(BA)/Co(2)

a_1	3.4895	0	0	3.4895	0	0	a_1	3.4814	0	0
a_2	0	6.254	0	0	6.254	0	a_2	0	6.3562	0
a_3	0	0	45	0	0	45	a_3	0	0	39.9653
W	0.0	0.0628	0.4207	0.5	0.9473	0.4207	Mo	0.5	0.1807	0.5489
W	0.5	0.9466	0.2680	0.0	0.5929	0.4161	Mo	0.0	0.8196	0.5442
W	0.0	0.5917	0.2641	0.0	0.0629	0.2677	Mo	0.0	0.3294	0.3829
W	0.5	0.4171	0.4161	0.5	0.4177	0.2639	Mo	0.5	0.6967	0.3794
Te	0.0	0.1992	0.2337	0.5	0.3436	0.4505	Te	0.0	0.0782	0.5972
Te	0.5	0.8134	0.3869	0.0	0.8508	0.4642	Te	0.5	0.5722	0.5824
Te	0.0	0.3211	0.3725	0.0	0.1968	0.3869	Te	0.0	0.4292	0.5120
Te	0.5	0.6877	0.2196	0.5	0.6895	0.3725	Te	0.5	0.9224	0.4958
Te	0.0	0.6667	0.4506	0.0	0.6655	0.2973	Te	0.5	0.4323	0.4316
Te	0.5	0.3441	0.2975	0.5	0.1579	0.3117	Te	0.0	0.9406	0.4160
Te	0.0	0.8515	0.3120	0.5	0.8104	0.2335	Te	0.5	0.0807	0.3450
Te	0.5	0.1589	0.4642	0.0	0.3218	0.2194	Te	0.0	0.5921	0.3301
Co	0.5	0.9424	0.1750	0.5	0.8206	0.1779	Co	0.5	1.0775	0.2826
Co	0.0	0.6844	0.1746	0.0	0.5807	0.1744	Co	0.5	0.5883	0.2808
Co	0.5	0.4258	0.1749	0.5	0.3225	0.1744	Co	0.0	0.3233	0.2824
Co	0.0	0.1848	0.1780	0.0	0.0632	0.1751	Co	0.0	0.8416	0.2789
Co	0.0	0.4250	0.1372	0.0	0.3204	0.1378	Co	0.5	0.3285	0.2402
Co	0.0	0.9428	0.1374	0.0	0.8227	0.1364	Co	0.0	0.5758	0.2398
Co	0.5	0.6843	0.1380	0.5	0.5814	0.1369	Co	0.5	0.8385	0.2374
Co	0.5	0.1845	0.1367	0.5	0.0630	0.1375	Co	0.0	1.0891	0.2378

[1] A. Manchon and S. Zhang, Physical Review B **79**, 094422 (2009).

[2] L. Liu, T. Moriyama, D. Ralph, and R. Buhrman, Physical review letters **106**, 036601 (2011).

[3] I. M. Miron, K. Garello, G. Gaudin, P.-J. Zermatten, M. V. Costache, S. Auffret, S. Bandiera, B. Rodmacq, A. Schuhl, and P. Gambardella, Nature **476**, 189 (2011).

[4] A. Manchon, J. Železnỳ, I. M. Miron, T. Jungwirth, J. Sinova, A. Thiaville, K. Garello, and P. Gambardella, Reviews of Modern Physics **91**, 035004 (2019).

[5] D. C. Ralph and M. D. Stiles, Journal of Magnetism and Magnetic Materials **320**, 1190 (2008).

[6] L. Liu, C.-F. Pai, Y. Li, H. Tseng, D. Ralph, and R. Buhrman, Science **336**, 555 (2012).

[7] K. Garello, I. M. Miron, C. O. Avci, F. Freimuth, Y. Mokrousov, S. Blügel, S. Auffret, O. Boulle, G. Gaudin, and P. Gambardella, Nature Nanotechnology **8**, 587 (2013).

[8] C.-F. Pai, L. Liu, Y. Li, H. Tseng, D. Ralph, and R. Buhrman, Applied Physics Letters **101**, 122404 (2012).

[9] K. Wang, J. Alzate, and P. K. Amiri, Journal of Physics D: Applied Physics **46**, 074003 (2013).

[10] K. Garello, C. O. Avci, I. M. Miron, M. Baumgartner, A. Ghosh, S. Auffret, O. Boulle, G. Gaudin, and P. Gam-

bardella, Applied Physics Letters **105**, 212402 (2014).
[11] L. Liu, O. Lee, T. Gudmundsen, D. Ralph, and R. Buhrman, Physical review letters **109**, 096602 (2012).
[12] M. Cubukcu, O. Boulle, M. Drouard, K. Garello, C. Onur Avci, I. Mihai Miron, J. Langer, B. Ocker, P. Gambardella, and G. Gaudin, Applied Physics Letters **104**, 042406 (2014).
[13] Y.-C. Lau, D. Betto, K. Rode, J. Coey, and P. Stamenov, Nature nanotechnology **11**, 758 (2016).
[14] C. B. Seung-heon, V. P. Amin, Y.-W. Oh, G. Go, S.-J. Lee, G.-H. Lee, K.-J. Kim, M. D. Stiles, B.-G. Park, and K.-J. Lee, Nature materials **17**, 509 (2018).
[15] S. Fukami, C. Zhang, S. DuttaGupta, A. Kurenkov, and H. Ohno, Nature materials **15**, 535 (2016).
[16] Y.-W. Oh, S.-h. C. Baek, Y. Kim, H. Y. Lee, K.-D. Lee, C.-G. Yang, E.-S. Park, K.-S. Lee, K.-W. Kim, G. Go, *et al.*, Nature nanotechnology **11**, 878 (2016).
[17] G. Yu, P. Upadhyaya, Y. Fan, J. G. Alzate, W. Jiang, K. L. Wong, S. Takei, S. A. Bender, L.-T. Chang, Y. Jiang, *et al.*, Nature nanotechnology **9**, 548 (2014).
[18] D. MacNeill, G. M. Stiehl, M. H. D. Guimaraes, R. A. Buhrman, J. Park, and D. C. Ralph, Nature Physics **13**, 300 (2016).
[19] D. MacNeill, G. M. Stiehl, M. H. D. Guimarães, N. D. Reynolds, R. A. Buhrman, and D. C. Ralph, Phys. Rev. B **96**, 054450 (2017).
[20] G. M. Stiehl, D. MacNeill, N. Sivadas, I. El Baggari, M. H. D. Guimarães, N. D. Reynolds, L. F. Kourkoutis, C. J. Fennie, R. A. Buhrman, and D. C. Ralph, ACS Nano **13**, 2599 (2019).
[21] G. M. Stiehl, R. Li, V. Gupta, I. E. Baggari, S. Jiang, H. Xie, L. F. Kourkoutis, K. F. Mak, J. Shan, R. A. Buhrman, and D. C. Ralph, Phys. Rev. B **100**, 184402 (2019).
[22] L. Fernández-Seivane, M. A. Oliveira, S. Sanvito, and J. Ferrer, Journal of Physics: Condensed Matter **18**, 7999 (2006).
[23] P. M. Haney, H.-W. Lee, K.-J. Lee, A. Manchon, and M. D. Stiles, Phys. Rev. B **88**, 214417 (2013).
[24] F. Freimuth, S. Blügel, and Y. Mokrousov, Phys. Rev. B **90**, 174423 (2014).
[25] J. Sinova, D. Culcer, Q. Niu, N. A. Sinitsyn, T. Jungwirth, and A. H. MacDonald, Phys. Rev. Lett. **92**, 126603 (2004).
[26] N. Nagaosa, J. Sinova, S. Onoda, A. H. MacDonald, and N. P. Ong, Rev. Mod. Phys. **82**, 1539 (2010).
[27] J. Sinova, S. O. Valenzuela, J. Wunderlich, C. H. Back, and T. Jungwirth, Rev. Mod. Phys. **87**, 1213 (2015).
[28] J. H. Ryoo, C.-H. Park, and I. Souza, Phys. Rev. B **99**, 235113 (2019).
[29] The code used to evaluate Eqs. 3 and 4 is available from the corresponding authors upon reasonable request.
[30] G. Kresse and J. Furthmüller, Phys. Rev. B **54**, 11169 (1996).
[31] Disclaimer: Certain commercial products are identified in this paper in order to specify the theoretical procedure adequately. Such identification is not intended to imply recommendation or endorsement by the National Institute of Standards and Technology nor is it intended to imply that the software identified is necessarily the best available for the type of work.
[32] P. Giannozzi, O. Andreussi, T. Brumme, O. Bunau, M. B. Nardelli, M. Calandra, R. Car, C. Cavazzoni, D. Ceresoli, M. Cococcioni, N. Colonna, I. Carnimeo, A. D. Corso, S. de Gironcoli, P. Delugas, R. A. DiStasio, A. Ferretti, A. Floris, G. Fratesi, G. Fugallo, R. Gebauer, U. Gerstmann, F. Giustino, T. Gorni, J. Jia, M. Kawamura, H.-Y. Ko, A. Kokalj, E. Kçkbenli, M. Lazzeri, M. Marsili, N. Marzari, F. Mauri, N. L. Nguyen, H.-V. Nguyen, A. O. de-la Roza, L. Paulatto, S. Poncé, D. Rocca, R. Sabatini, B. Santra, M. Schlipf, A. P. Seitsonen, A. Smogunov, I. Timrov, T. Thonhauser, P. Umari, N. Vast, X. Wu, and S. Baroni, Journal of Physics: Condensed Matter **29**, 465901 (2017).
[33] G. Kresse and D. Joubert, Phys. Rev. B **59**, 1758 (1999).
[34] J. P. Perdew, K. Burke, and M. Ernzerhof, Phys. Rev. Lett. **77**, 3865 (1996).
[35] H. J. Monkhorst and J. D. Pack, Phys. Rev. B **13**, 5188 (1976).
[36] S. Grimme, Journal of Computational Chemistry **27**, 1787 (2006), https://onlinelibrary.wiley.com/doi/pdf/10.1002/jcc.20495.
[37] A. A. Mostofi, J. R. Yates, G. Pizzi, Y.-S. Lee, I. Souza, D. Vanderbilt, and N. Marzari, Computer Physics Communications **185**, 2309 (2014).
[38] D. Gresch, Q. Wu, G. W. Winkler, R. Häuselmann, M. Troyer, and A. A. Soluyanov, Phys. Rev. Materials **2**, 103805 (2018).
[39] K. D. Belashchenko, A. A. Kovalev, and M. van Schilfgaarde, Phys. Rev. Materials **3**, 011401 (2019).
[40] F. J. Sousa, G. Tatara, and A. Ferreira, Emergent spin-orbit torques in two-dimensional material/ferromagnet interfaces (2020), arXiv:2005.09670 [cond-mat.mes-hall].
[41] F. Mahfouzi and N. Kioussis, Phys. Rev. B **97**, 224426 (2018).
[42] D. Go, F. Freimuth, J.-P. Hanke, F. Xue, O. Gomonay, K.-J. Lee, S. Blgel, H.-W. Lee, and Y. Mokrousov, First-principles theory of current-induced spin-orbital coupled dynamics in magnetic heterostructures (2020), arXiv:2004.05945 [cond-mat.mes-hall].
[43] D. Go and H.-W. Lee, Physical Review Research **2**, 013177 (2020).
[44] L. M. Canonico, T. P. Cysne, A. Molina-Sanchez, R. B. Muniz, and T. G. Rappoport, Phys. Rev. B **101**, 161409 (2020).
[45] W. Wang, T. Wang, V. P. Amin, Y. Wang, A. Radhakrishnan, A. Davidson, S. R. Allen, T. J. Silva, H. Ohldag, D. Balzar, *et al.*, Nature nanotechnology **14**, 819 (2019).
[46] V. P. Amin, J. Zemen, and M. D. Stiles, Physical review letters **121**, 136805 (2018).
[47] P. M. Haney and M. D. Stiles, Physical review letters **105**, 126602 (2010).
[48] J. Zhou, J. Qiao, A. Bournel, and W. Zhao, Phys. Rev. B **99**, 060408 (2019).
[49] X. Zhang, Q. Liu, J.-W. Luo, A. J. Freeman, and A. Zunger, Nature Physics **10**, 387 (2014).
[50] P. Wadley, B. Howells, J. Železnỳ, C. Andrews, V. Hills, R. P. Campion, V. Novák, K. Olejník, F. Maccherozzi, S. Dhesi, *et al.*, Science **351**, 587 (2016).
[51] M.-H. Nguyen, D. Ralph, and R. Buhrman, Physical review letters **116**, 126601 (2016).
[52] L. Zhu, D. Ralph, and R. Buhrman, Physical review letters **122**, 077201 (2019).
[53] S. Shi, S. Liang, Z. Zhu, K. Cai, S. D. Pollard, Y. Wang, J. Wang, Q. Wang, P. He, J. Yu, *et al.*, Nature nanotechnology **14**, 945 (2019).
[54] P. Li, W. Wu, Y. Wen, C. Zhang, J. Zhang, S. Zhang, Z. Yu, S. A. Yang, A. Manchon, and X.-x. Zhang, Nature communications **9**, 1 (2018).

[55] Q. Shao, G. Yu, Y.-W. Lan, Y. Shi, M.-Y. Li, C. Zheng, X. Zhu, L.-J. Li, P. K. Amiri, and K. L. Wang, Nano letters **16**, 7514 (2016).